Chen, Guannan ; Howard, Sean; Maghirang, A; Cong, K N; Villaos, R. A. B; Feng, L. Y.; Cai, K; Ganguli, Somesh; Swiech, W; Morosan, E; Oleynik, R; Chuang, F. C.; Lin, H; Madhavan, V

Correlating structural, electronic, and magnetic properties of epitaxial VSe2 thin films

Published in:
Physical Review B (Condensed Matter and Materials Physics)

DOI:
10.1103/PhysRevB.102.115149

Published: 23/09/2020

Document Version
Publisher's PDF, also known as Version of record

Please cite the original version:
Chen, G., Howard, S., Maghirang, A., Cong, K. N., Villaos, R. A. B., Feng, L. Y., Cai, K., Ganguli, S., Swiech, W., Morosan, E., Oleynik, R., Chuang, F. C., Lin, H., & Madhavan, V. (2020). Correlating structural, electronic, and magnetic properties of epitaxial VSe2 thin films. *Physical Review B (Condensed Matter and Materials Physics)*, *102*(11), 1-6. Article 115149. https://doi.org/10.1103/PhysRevB.102.115149

Editors' Suggestion

Correlating structural, electronic, and magnetic properties of epitaxial VSe_2 thin films

Guannan Chen,[1,2] Sean T. Howard,[1,2] Aniceto B. Maghirang III,[3] Kien Nguyen Cong,[4] Rovi Angelo B. Villaos,[3] Liang-Ying Feng,[3] Kehan Cai,[5] Somesh C. Ganguli,[6] Waclaw Swiech,[2] Emilia Morosan,[7] Ivan I. Oleynik,[4] Feng-Chuan Chuang,[3] Hsin Lin,[8] and Vidya Madhavan[1,2]

[1]*Department of Physics, University of Illinois Urbana-Champaign, Urbana, Illinois 61801, USA*
[2]*Materials Research Laboratory, University of Illinois Urbana-Champaign, Urbana, Illinois 61801, USA*
[3]*Department of Physics, National Sun Yat-sen University, Kaohsiung 80424, Taiwan*
[4]*Department of Physics, University of South Florida, Tampa, Florida 33620, USA*
[5]*Department of Chemistry, Princeton University, Princeton, New Jersey 08544, USA*
[6]*Department of Applied Physics, Aalto University School of Science, P.O. Box 11100, 00076 Aalto, Finland*
[7]*Department of Physics and Astronomy and Rice Center for Quantum Materials, Rice University, Houston, Texas 77005, USA*
[8]*Institute of Physics, Academia Sinica, Taipei 11529, Taiwan*

(Received 15 December 2019; revised 8 July 2020; accepted 14 August 2020; published 23 September 2020)

The electronic and magnetic properties of transition metal dichalcogenides are known to be extremely sensitive to their structure. In this paper we study the effect of structure on the electronic and magnetic properties of mono- and bilayer VSe_2 films grown using molecular beam epitaxy. VSe_2 has recently attracted much attention due to reports of emergent ferromagnetism in the two-dimensional (2D) limit. To understand this compound, high-quality 1*T* and distorted 1*T* films were grown at temperatures of 200 °C and 450 °C, respectively, and studied using 4 K scanning tunneling microscopy and spectroscopy. The measured density of states and the charge density wave (CDW) patterns were compared to band structure and phonon dispersion calculations. Films in the 1*T* phase reveal different CDW patterns in the first layer compared to the second. Interestingly, we find the second layer of the 1*T* film shows a CDW pattern with $4a \times 4a$ periodicity which is the 2D version of the bulk CDW observed in this compound. Our phonon dispersion calculations confirm the presence of a soft phonon at the correct wave vector that leads to this CDW. In contrast, the first layer of distorted 1*T* phase films shows a strong stripe feature with varying periodicities, while the second layer displays no observable CDW pattern. Finally, we find that the monolayer 1*T* VSe_2 film is weakly ferromagnetic, with ~3.5 μ_B per unit similar to previous reports.

DOI: 10.1103/PhysRevB.102.115149

I. INTRODUCTION

Two-dimensional (2D) materials such as graphene have attracted much recent attention due to the novel electronic and physical properties that accompany reduced dimensionality. While graphene has a large range of potential applications, the lack of an electronic band gap limits its use in optical and semiconducting devices [1]. Another 2D material system of interest is transition metal dichalcogenides (TMDs). TMDs are layered materials containing two chalcogen atoms per transition metal atom, displaying strong intralayer bonding and weak van der Waals interlayer bonding. The weak interlayer bonding of TMDs facilitates control of film thickness via growth or exfoliation down to submonolayer. As TMDs are reduced to 2D, novel physics often emerges such as itinerant magnetism [2], an indirect to direct band-gap transition [3,4], quantum spin Hall effect [5], and strongly enhanced charge density wave (CDW) order [6]. This breadth of phenomena makes 2D TMDs a promising platform both for the development of next generation devices and important fundamental studies.

VSe_2 has recently attracted much interest due to reports of emergent room temperature ferromagnetism in the 2D limit. This finding, however, remains controversial as several theoretical [7–10] and experimental [11–13] studies both confirm and deny the possibility of a ferromagnetic phase in this compound. The films are also interesting due to the variety of CDW patterns observed which are distinct from the bulk sample [14,15], raising questions about the role of Fermi surface nesting and phonons in CDW formation. Bulk VSe_2 is paramagnetic [16–18] and noteworthy for being one of the few materials exhibiting a three-dimensional CDW ($4a \times 4a \times 3.1c$) [19]. The bulk material has been shown to be stable in 1*T* octahedral structure [Figs. 1(a) and 1(b)]. In general, however, TMDs can also be found in 2*H* trigonal prismatic structure and distorted 1*T* structure [Figs. 1(c) and 1(d)], including $1T_d$ orthorhombic and 1*T*′ monoclinic, which occurs when the chalcogen atoms in the 1*T* phase dimerize [1,20]. Most reports of 2D VSe_2 films have been carried out on the 1*T* phase, leaving the synthesis and electronic properties of other polymorphs largely unexplored.

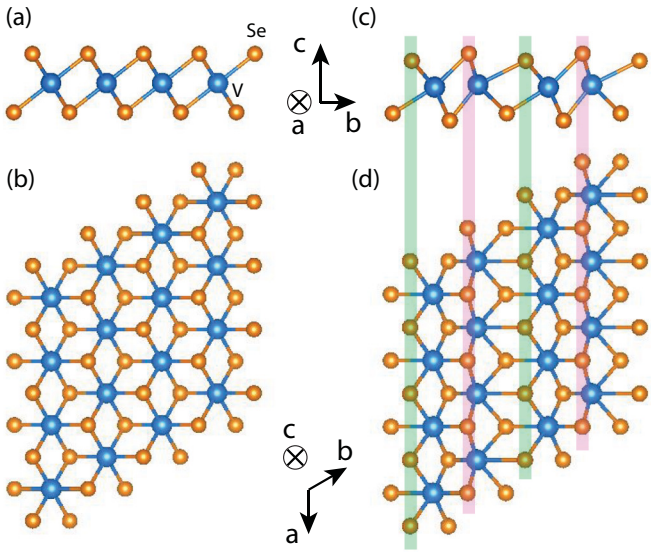

FIG. 1. Schematic structure of 1*T* and distorted 1*T* VSe_2. The blue circles represent V atoms and the orange circles represent Se atoms. (a) Side view and (b) top view of 1*T*-VSe_2. (c) Side view and (d) top view of distorted 1*T*-VSe_2. The green and pink ribbons highlight the lower and higher top Se atoms, correspondingly.

In this paper we report the molecular beam epitaxy (MBE) growth of VSe_2 films on bilayer graphene (BLG)/6H-SiC (0001) substrates at two different growth temperatures, resulting in two distinct polymorphs. The synthesis procedures were characterized with reflection high-energy electron diffraction (RHEED) and scanning tunneling microscopy (STM) to discern structural and electronic properties compared to bulk VSe_2 crystals. At lower growth temperatures of 200 °C, the monolayer film displays the 1*T* phase, which exhibits unique incommensurate CDW patterns in contrast to previous reports [11,13,14,21,22]. Interestingly, the CDW in the bilayer is a two-dimensional projection of the commensurate bulk CDW structure. For the higher growth temperature of 450 °C, a striped discommensurate CDW in the monolayer is revealed which is a precursor to the distorted 1*T* phase [Figs. 1(c) and 1(d)] observed in the bilayer. Our magnetization measurements show that the monolayer VSe_2 samples grown at low temperature are weakly ferromagnetic with Curie temperature higher than 300 K. Intriguingly, the 1.5-layer VSe_2 samples grown at higher temperature also exhibit ferromagnetic behavior at room temperature or below, but with a lower magnetic moment per V atom.

II. METHODS

VSe_2 thin films were grown on bilayer graphene (BLG) on SiC using a home-built MBE system with a base pressure $<1 \times 10^{-9}$ Torr. For BLG growth, 6H-SiC (0001) substrates were washed in acetone and isopropanol and then loaded into the MBE chamber. The substrates were degassed at 650 °C for 2–3 h, then flash annealed 45 times between 650 °C and 1300 °C. High-purity V (99.8%) and Se (99.999%) were evaporated from an *e*-beam evaporator and a dual-filament low-temperature Knudsen cell, respectively. The fluxes of V and Se were measured by a quartz crystal monitor, with the flux ratio kept between 1:20 and 1: 30. The growth processes were monitored by *in situ* RHEED. The thin films grown at 200 °C and 450 °C are labeled low growth temperature (LGT) samples and high growth temperature (HGT) samples, respectively.

After growth, the samples were transferred to a low-temperature scanning tunneling microscope (STM) using a home-built "vacuum suitcase" to prevent the degradation of the sample quality. The vacuum during the transfer was less than 1×10^{-9} Torr. STM and scanning tunneling spectroscopy (STS) measurements were performed at 4 K. In the STM measurements, electrochemically etched and vacuum annealed tungsten tips were used. For comparison, bulk VSe_2 single crystals were cleaved *in situ* at a base pressure $<2 \times 10^{-9}$ Torr and transferred into the same low-temperature STM.

To carry out measurements of the films' magnetic properties, they were capped with 10 nm of amorphous Se immediately after growth. The samples were then taken out of the MBE chamber and mounted into the Quantum Design Magnetic Properties Measurement System (MPMS). The magnetization *M-H* curves were measured in superconducting quantum interference device (SQUID) vibrating sample magnetometer (VSM) mode with an in-plane magnetic field. The magnetic moment per formula unit is roughly estimated by dividing the saturation magnetization, converted to Bohr magnetons, by the number of formula units which is obtained from the surface area, thickness, and volume of the VSe_2 unit cell.

The first-principles calculations were carried out using the Vienna *ab initio* simulation package (VASP) [23,24] with the projected augmented wave (PAW) [25] potentials. The exchange-correlation functional was treated within the Perdew-Burke-Ernzerhof (PBE) generalized gradient approximations (GGA) [26–30]. The cutoff energy used throughout the calculations was set to 400 eV. Atomic positions were optimized for each lattice constant value considered until the residual forces were no greater than 10^{-3} eV/Å. The criteria for energy convergence for self-consistency was set at 10^{-6} eV . The vacuum region along the z direction was set to approximately 15 Å to prevent interactions between the repeated monolayer/bilayer slabs under the periodic boundary condition. A Γ-centered Monkhorst-Pack [31] grid of $12 \times 12 \times 1$ in the first Brillouin zone was used for calculating atomic structures and lattice relaxations. However, a denser grid of $36 \times 36 \times 1$ was used for density of states calculations.

To investigate lattice dynamics, phonon dispersion is calculated using the supercell method as implemented in the PHONOPY code [32]. We consider 4×4 supercells and 1×1 cells for phonon calculations of 1*T* and 4×4 CDW structures, respectively. Crystal structure of 4×4 CDW is determined by displaying atoms of a 4×4 perfect 1*T* supercell along the eigenvector of a soft mode at a commensurate q point followed by atomic relaxation in the fixed supercell.

III. RESULTS AND DISCUSSION

Previous works on VSe_2 thin films report several distinct CDW patterns, as well as the existence and absence of ferromagnetism, which highlight the sensitivity of resultant

film properties to growth parameters and substrate choices [11,13–15]. The exploration of the substrate and synthesis parameter space is therefore important in fine-tuning film properties. BLG was chosen as a substrate in hopes of approximating a free-standing film for two reasons. First, as graphene does not have a Fermi surface near the Γ point where VSe_2 has a holelike band, substrate-film interaction could be minimized. Second, a large lattice mismatch between graphene and Se lattice encourages weak van der Waals bonding between BLG and the film. However, a previous study on VSe_2 thin films [14] reported a dependence of the CDW structure on the relative angle between the substrate and film. Therefore, heterostructure effects cannot be completely neglected.

Two different synthesis conditions were used in our experiments; LGT, where the substrate was held at 200 °C, and HGT, where the substrate was held at 450 °C. The BLG grown on SiC is atomically flat, observed by RHEED, whose pattern is shown in Fig. 2(a). High-quality 2D growth is confirmed with sharp streaks in RHEED images [Fig. 2(b)], which are seen for the 0.5 layer at both growth temperatures. A growth rate of 0.06 layer/min allowed for control of film thickness. Since our studies focused on the first and second layers, we aimed for 1.5-layer film growth in both conditions which allows us to see both the first and the second layers. Both growth procedures produced large terraces of VSe_2 on BLG [Figs. 2(e) and 2(g)].

The 1.5-layer LGT film, as shown in Fig. 2(c), displays the same RHEED pattern as the 0.5-layer film. The absence of a graphene RHEED pattern indicates an almost complete coverage of the substrate by the film. STM images of the 1.5-layer LGT film show a triangular Se lattice with lattice constant $a = 0.34$ nm [Figs. 3(a) and 3(d)], which is consistent with the bulk lattice constant as well as with other reports of VSe_2 films [19,33]. In the region where multiple layers (including a small exposed BLG area) are visible, a line-cut profile across the edges is shown in Fig. 2(f) [the orange line in Fig. 2(e)]. A step height of 0.6 nm is seen between the first and second layer of VSe_2, consistent with the c-axis lattice constant in the bulk of 0.61 nm [33]. On the other hand, the height difference between BLG and the first layer is 0.8 nm, which is slightly larger than the lattice constant c in the bulk VSe_2. This is consistent with previous experimental reports [34,35] and can be identified as a monolayer since 0.8 nm is significantly closer to monolayer (0.61 nm) thickness than the two-layer thickness (1.22 nm). This difference in heights is likely due to interfacial effects.

STM images on the monolayer reveal several 2D CDW patterns in different areas (Supplemental Fig. 1 in the Supplemental Material [36]). The most frequently observed CDW is shown in Fig. 3(a) with CDW vectors of $q_1 = 4.2a$ by $q_2 = 4.6a$, approximately. This 2D CDW order forms an oblique lattice with an angle of approximately 114° and displays minor variations in the angle and magnitude in different areas on the sample. The 2D CDW is concomitant with a strong incommensurate 1D stripe order of periodicity $d = 0.79$ nm equivalent to $2.33a$. The 1D order occurs at an angle that is approximately 30° deviated from one of the Se lattice directions and is observed in all monolayer scans with the same angle and periodicity. The 1D feature may perhaps be attributed

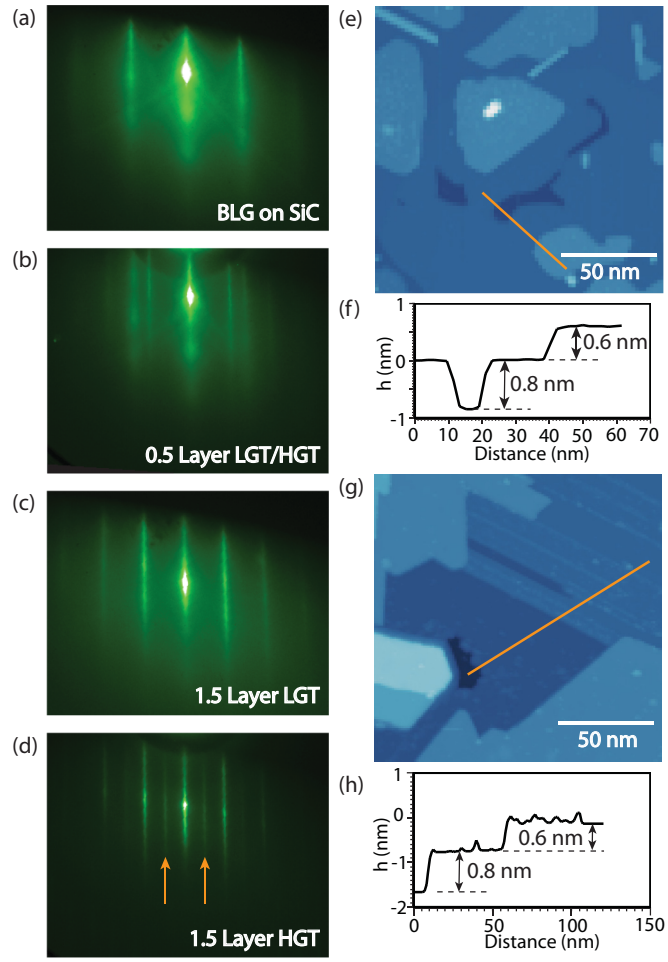

FIG. 2. Characterization of epitaxially grown VSe_2 films by RHEED and STM. (a)–(d) RHEED pattern of BLG grown on 6H-SiC (0001) substrate, LGT and HGT films after 0.5-layer growth, LGT film after 1.5-layer deposition, and HGT film after 1.5-layer deposition. In (d) the extra streaks are marked by the orange arrows, which indicate the formation of the distorted 1T phase. (e), (g) Large STM topographies of 1.5-layer LGT and 1.5-layer HGT samples (150 nm × 150 nm). (f), (h) Height profiles of the orange lines in (e), (g), respectively.

to a mixture of $\sqrt{3}a \times \sqrt{7}a$ and $\sqrt{3}a \times 2a$ CDW patterns. Previous reports of coexisting $\sqrt{3}a \times \sqrt{7}a$ and $\sqrt{3}a \times 2a$ CDW orders in VSe_2 thin films [14] show peaks in the Fourier transform at a period of $2.28a$ which is close to the $2.33a$ periodicity observed by us in this region. The observation of coexisting CDWs is also consistent with first-principles phonon calculations for the 1T monolayer which show multiple potential CDW instabilities corresponding to commensurate and incommensurate $4a \times 4a$ (q_1 and q_2), $\sqrt{3}a \times \sqrt{7}a$ (q_4), and $\sqrt{7}a \times \sqrt{7}a$ (q_5) structures [Fig. 3(b)]. We note that consistent with previous studies on VSe_2 films, the monolayer does not show a moiré pattern which based on the lattice mismatch would be expected to have a $3a \times 3a$ periodicity. Finally, as shown in Fig. 3(c), a measurement of the density of states of the LGT monolayer by STM spectroscopy shows a gap of 52 ±2 meV centered at the Fermi energy (also see Supplemental Fig. 2 [36]). Using a Bardeen–Cooper–Schrieffer

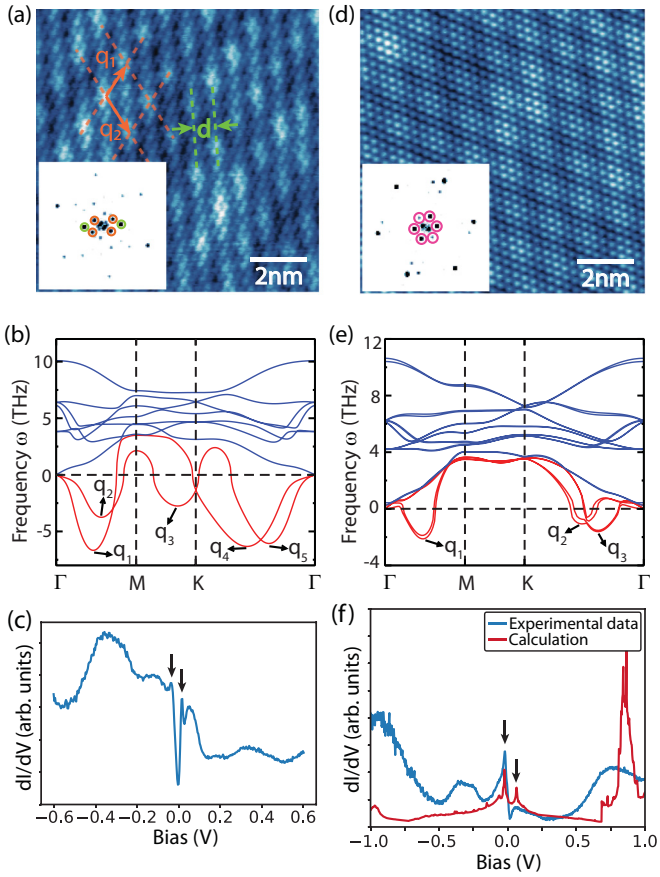

FIG. 3. STM data on first- and second-layer LGT VSe_2 films. (a) Atomic resolution STM topography of the first layer in LGT sample (10 nm × 10 nm). The 2D CDW vectors are shown as the orange arrows and green lines indicate the 1D stripe order with periodicity d. Inset: 2D fast Fourier transform (FFT). The orange and green circles represent the 2D CDW order and 1D stripe order, respectively. (b) Calculated phonon dispersion relations for monolayer 1T VSe_2. (c) The typical *dI/dV* spectrum of the first layer LGT. The vertical arrows correspond to peaks at −32 and +18 meV. (d) The atomic resolution STM topography of the second layer in LGT sample (10 nm × 10 nm) with 2D FFT as inset. The pink circles in the FFT indicate the peaks associated with $4a \times 4a$ CDW. (e) Calculated phonon dispersion relations for bilayer VSe_2. (f) Comparison of *dI/dV* spectra of the second layer of LGT sample (blue line) and density of state curve from first-principles calculation (red line). The arrows indicate the peaks in the calculated density of states at −25 and +62 meV, very similar to the experimental data.

(BCS) – like formula $T_{CDW} = 2\Delta/3.52k_B$ a weak coupling estimate can be obtained for the CDW transition temperature T_{CDW}. Given the average gap size $2\Delta = 52$ meV, we obtain a T_{CDW} of ∼171 K. The CDW transition temperature reported previously ranges from 120 to 350 K for monolayer 1*T*-VSe_2 samples [11,13,14,21]. The gap size and estimated T_{CDW} from our data are therefore reasonable. It is also important to note that while the differential conductance at the zero bias is significantly suppressed, it is nonzero as seen in Fig. 3(c). This soft gap is not seen in our DFT calculations (Supplemental Fig. 3 [36]) and is likely associated with the CDWs observed in the film.

Surprisingly, the bilayer LGT sample hosts a CDW which resembles the bulk (Supplemental Fig. 4(a) [36]) displaying a commensurate 2D CDW pattern with $4a \times 4a$ periodicity [Fig. 3(d)]. Our phonon dispersion calculations [Fig. 3(e)] display three noticeable imaginary modes at q_1, q_2, and q_3. The mode at $q_1 \sim -1/2\,\overline{\Gamma M}$ has the largest negative frequency, and the displacing atom along the eigenvector of this mode results in a $4a \times 4a$ commensurate CDW structure. According to our calculation, the energy of this CDW state is 11 meV/atom lower than that of the normal state. Thus, the $4a \times 4a$ CDW is indeed preferred in this system and the electron-phonon interaction plays an important role in its formation. Moving on to density of states measurements as shown by the blue curve in Fig. 3(f), we observe a large peak around −22 meV which is absent in the monolayer (Supplemental Fig. 5 [36]). To understand these data, we performed the first-principles calculations for the bilayer which is shown as the red curve in Fig. 3(f). The calculation fits reasonably well with the experimental data in terms of the energy scales of some of the important features. The peaks around −25 and + 62 meV in the calculated density of states match the experimental peaks at −22 and +60 meV. These arise from the 3*d* bands of V which are split due to the bilayer coupling and this assignment of the peak to V *d* bands is confirmed by a comparison of the second-layer spectrum and the STM measured density of states (DOS) of the bulk sample (Supplemental Fig. 4(b) [36]). A similar peak feature appears in the bulk but is sharper in the bilayer. A comparison of the bilayer to the monolayer in the LGT films thus demonstrates the significant impact of just one additional layer of growth on phonons as well as the band structure.

The HGT films obtained by changing the substrate growth temperature by a few hundred degrees exhibit drastically different properties. Before proceeding we note that even though the growth temperature is higher, by keeping the Se to V flux ratio very high, between 20 and 30, we avoid Se loss in the films. Correspondingly our topographies of all HGT films show the expected hexagonal Se lattice with no missing Se atoms. We start by studying the HGT monolayer. While RHEED images of the monolayer look identical to the LGT [Fig. 2(b)], STM images show a strong 1D stripe feature with varying periodicity. As seen in Fig. 4(a), the stripes occur along a lattice direction with periodicities of either 4, 5, or 6 times the lattice. Along the direction of stripes, the lattice constant, 0.34 nm, is the same as the one in LGT samples. Taking a line cut along the stripe direction [Fig. 4(e)], it is clear that the distances between two adjacent atoms are uniform. However, along the other two lattice directions [the height profile shown in Fig. 4(f)], it appears that the atoms are not evenly spaced and the average atomic separation, 0.31 nm, is almost 10% smaller than the one along the stripes and in LGT samples. To confirm the universality of this observation, we obtained topographies in different areas with stripes along various directions. We find that the difference between lattice constants along and across the stripe direction is consistent. Interestingly, the spectra on bright and dark stripes are different (Supplemental Fig. 6 [36]) which suggests an electronic origin (such as a CDW) for the stripes. One-dimensional CDWs with varying periodicities have been explained using the theory of discommensurations, where

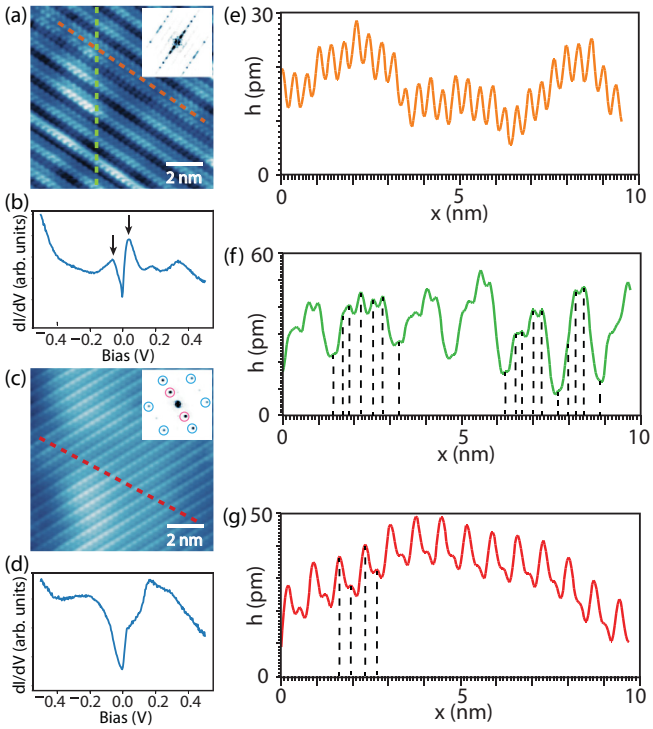

FIG. 4. STM data on first layer and second layer of the HGT VSe_2 film. (a), (c) STM topographic images of the first layer and second layer of HGT samples (10 nm × 10 nm). The insets are the corresponding 2D FFT images. In (c) the blue and pink circles highlight the peaks related with the top Se lattice (blue) and stripes caused by the structural distortion (pink). (b), (d) Typical dI/dV curves measured on the first layer and second layer of HGT VSe_2 films, respectively. The arrows in (b) indicate peaks at −56 and +36 meV. (e)–(g) The height profiles of the orange and green line in (a) and red line in (c), respectively. In (f), (g), the black dashed lines show the positions of atoms.

slightly incommensurate CDWs become commensurate over a region and undergo a phase slip between regions to lower their energy [37]. Discommensurate CDWs have been previously observed in bulk $NbSe_2$, caused by local strain [38]. In our HGT VSe_2 samples, we speculate that strain induced by synthesis conditions or growth specific heterostructure interactions may cause dimerization and discommensurate CDW in the monolayer. We note that a discommensurate 1D CDW has not been observed in previous VSe_2 monolayer studies.

As the growth progresses from monolayer to bilayer, accompanying the HGT bilayer growth are additional streaks in the RHEED image, as shown in Fig. 2(d). These streaks occur halfway between the center spot and the most prominent RHEED streaks, implying the onset of a $2a$ structural periodicity. Correspondingly, STM images of the HGT bilayer show a one-dimensional pattern along a lattice direction [Fig. 4(c)]. The RHEED pattern, STM images, and previous reports on $1T'$ TMDs [5,39] lead us to conclude that the bilayer HGT film grows in the distorted $1T$ phase. As illustrated in Figs. 1(c) and 1(d), the V atoms in the distorted $1T$ phase dimerize, causing the bond lengths of neighboring Se atoms to change. Se atoms in the center of a V dimer are slightly elevated in the interlayer direction and Se atoms in between dimers are slightly depressed. This elevation and depression are responsible for the contrast seen in the STM image and are obviously exhibited in a line-cut profile Fig. 4(g). As shown in Supplemental Fig. 7 [36], the spectra are almost identical across the stripes, consistent with our RHEED analysis that the stripes result from lattice distortion.

Though the structures of monolayer and bilayer are remarkably different, their spectra are qualitatively similar [Figs. 4(b) and 4(d)]. There are three peaks above the Fermi energy at approximately the same positions in the two layers, although their relative intensities are different. Below the Fermi energy, however, the density of states curve in the second layer is slightly different from the monolayer. We also carried out first-principles calculation for $1T'$ and $1T_d$ phase bilayer VSe_2. The comparison between experiment and calculation is shown in Supplemental Fig. 8 [36]. We find that unlike the calculations for the $1T$ films, the agreement between theory and experiment is not very good. One possible explanation is that the distorted $1T$ samples grow on a layer of strained $1T$ VSe_2, which the calculation does not capture.

Besides the electronic and structural properties of VSe_2 films in the atomic limit, the magnetic properties are also of significant interest. According to the M-H curves from MPMS measurements of our samples at different temperatures, the monolayer LGT VSe_2 sample is ferromagnetic, with ∼3.5 μ_B per formula unit similar to previous reports [14] and the Curie temperature is higher than 300 K. Intriguingly, the 1.5-layer HGT VSe_2 samples also exhibit a ferromagnetic behavior at room temperature or below, but with a weaker magnetic moment, ∼1.3 μ_B per formula unit. More details are displayed in Supplemental Fig. 9 [36].

IV. CONCLUSION

In this paper we report the growth of VSe_2 films on BLG/SiC at 200 °C and 450 °C, labeled LGT and HGT, respectively. The LGT films show 2D incommensurate CDW patterns in the monolayer, with a periodicity that is different from those of previous reports. This evolves into a commensurate $4a \times 4a$ CDW in the bilayer that is similar to the bulk. The HGT films show unique phenomenology when compared to the LGT films and previous reports. The HGT monolayer displays a 1D discommensurate CDW, indicative of strain. The HGT bilayer grows in the distorted $1T$ phase, which has, so far, rarely been reported in VSe_2 and is likely stabilized by interactions with the monolayer. Our results on the HGT films allow for the study of two interesting phenomena in VSe_2 films: a discommensurate 1D CDW and the distorted $1T$ phase. Specifically, the distorted $1T$ phase provides more possibilities for synthesizing different phases of TMDC thin films and realizing alternative heterostructures with potentially exotic properties.

ACKNOWLEDGMENTS

V.M. and E.M. acknowledge support from NSF DMREF Grant No. 1629068 and NSF DMREF Grant No. 1629374 for STM studies and sample characterization. MBE growth and characterization were supported by the Gordon and Betty

Moore Foundation's EPiQS Initiative through Grants No. GBMF4860 and No. GBMF9465. F.-C.C. acknowledges support from the National Center for Theoretical Sciences and the Ministry of Science and Technology of Taiwan under Grant No. MOST-107-2628-M-110-001-MY3. He is also grateful to the National Center for High-Performance Computing for computer time and facilities. The work at USF is supported by the DOE National Nuclear Security Administration Grant No. DE-NA0003910). Simulations were performed using the DOE leadership HPC supercomputer Summit at OLCF/ORNL (DOE ASCR ALCC award No. MAT198), and USF Research Computing Cluster CIRCE.

[1] S. Manzeli, D. Ovchinnikov, D. Pasquier, O. V. Yazyev, and A. Kis, Nat. Rev. Mater. **2**, 17033 (2017).
[2] T. Danz, Q. Liu, X. D. Zhu, L. H. Wang, S. W. Cheong, I. Radu, C. Ropers, and R. I. Tobey, J. Phys. Condens. Matter **28**, 356002 (2016).
[3] K. F. Mak, C. Lee, J. Hone, J. Shan, and T. F. Heinz, Phys. Rev. Lett. **105**, 136805 (2010).
[4] Y. Zhang, T.-R. Chang, B. Zhou, Y.-T. Cui, H. Yan, Z. Liu, F. Schmitt, J. Lee, R. Moore, Y. Chen *et al.*, Nat. Nanotechnol. **9**, 111 (2014).
[5] S. Tang, C. Zhang, D. Wong, Z. Pedramrazi, H.-Z. Tsai, C. Jia, B. Moritz, M. Claassen, H. Ryu, S. Kahn *et al.*, Nat. Phys. **13**, 683 (2017).
[6] X. Xi, L. Zhao, Z. Wang, H. Berger, L. Forró, J. Shan, and K. F. Mak, Nat. Nanotechnol. **10**, 765 (2015).
[7] Y. Ma, Y. Dai, M. Guo, C. Niu, Y. Zhu, and B. Huang, ACS Nano **6**, 1695 (2012).
[8] S. Lebègue, T. Björkman, M. Klintenberg, R. M. Nieminen, and O. Eriksson, Phys. Rev. X **3**, 031002 (2013).
[9] A. O. Fumega, M. Gobbi, P. Dreher, W. Wan, C. Gonzalez-Orellana, M. Peña-Diaz, C. Rogero, J. Herrero-Martin, P. Gargiani, M. Ilyn *et al.*, J. Phys. Chem. C **123**, 27802 (2019).
[10] P. Coelho, K. Nguyen-Cong, M. Bonilla, S. K. Kolekar, M.-H. Phan, J. Avila, M. C. Asensio, I. I. Oleynik, and M. Batzill, J. Phys. Chem. C **123**, 14089 (2019).
[11] M. Bonilla, S. Kolekar, Y. Ma, H. C. Diaz, V. Kalappattil, R. Das, T. Eggers, H. R. Gutierrez, M.-H. Phan, and M. Batzill, Nat. Nanotechnol. **13**, 289 (2018).
[12] K. Xu, P. Chen, X. Li, C. Wu, Y. Guo, J. Zhao, X. Wu, and Y. Xie, Angew. Chem., Int. Ed. **52**, 10477 (2013).
[13] J. Feng, D. Biswas, A. Rajan, M. D. Watson, F. Mazzola, O. J. Clark, K. Underwood, I. Markovic, M. McLaren, A. Hunter *et al.*, Nano Lett. **18**, 4493 (2018).
[14] G. Duvjir, B. K. Choi, I. Jang, S. Ulstrup, S. Kang, T. Thi Ly, S. Kim, Y. H. Choi, C. Jozwiak, A. Bostwick *et al.*, Nano Lett. **18**, 5432 (2018).
[15] D. Zhang, J. Ha, H. Baek, Y.-H. Chan, F. D. Natterer, A. F. Myers, J. D. Schumacher, W. G. Cullen, A. V. Davydov, Y. Kuk *et al.*, Phys. Rev. Mater. **1**, 024005 (2017).
[16] C. Van Bruggen and C. Haas, Solid State Commun. **20**, 251 (1976).
[17] M. Bayard and M. Sienko, J. Solid State Chem. **19**, 325 (1976).
[18] S. Barua, M. C. Hatnean, M. Lees, and G. Balakrishnan, Sci. Rep. **7**, 10964 (2017).
[19] A. Pasztor, A. Scarfato, C. Barreteau, E. Giannini, and C. Renner, 2D Mater. **4**, 041005 (2017).
[20] Q. H. Wang, K. Kalantar-Zadeh, A. Kis, J. N. Coleman, and M. S. Strano, Nat. Nanotechnol. **7**, 699 (2012).
[21] P. Chen, W. W. Pai, Y.-H. Chan, V. Madhavan, M.-Y. Chou, S.-K. Mo, A.-V. Fedorov, and T.-C. Chiang, Phys. Rev. Lett. **121**, 196402 (2018).
[22] Y. Umemoto, K. Sugawara, Y. Nakata, T. Takahashi, and T. Sato, Nano Res. **12**, 165 (2019).
[23] G. Kresse and J. Hafner, Phys. Rev. B **47**, 558 (1993).
[24] G. Kresse and J. Furthmuller, Phys. Rev. B **54**, 11169 (1996).
[25] G. Kresse and D. Joubert, Phys. Rev. B **59**, 1758 (1999).
[26] A. Rajagopal and J. Callaway, Phys. Rev. B **7**, 1912 (1973).
[27] W. Kohn and L. J. Sham, Phys. Rev. **140**, A1133 (1965).
[28] D. M. Ceperley and B. J. Alder, Phys. Rev. Lett. **45**, 566 (1980).
[29] J. P. Perdew and A. Zunger, Phys. Rev. B **23**, 5048 (1981).
[30] J. P. Perdew, K. Burke, and M. Ernzerhof, Phys. Rev. Lett. **77**, 3865 (1996).
[31] H. J. Monkhorst and J. D. Pack, Phys. Rev. B **13**, 5188 (1976).
[32] A. Togo and I. Tanaka, Scr. Mater. **108**, 1 (2015).
[33] J. A. Wilson and A. Yoffe, Adv. Phys. **18**, 193 (1969).
[34] Y. Zhao, J. Qiao, P. Yu, Z. Hu, Z. Lin, S. P. Lau, Z. Liu, W. Ji, and Y. Chai, Adv. Mater. **28**, 2399 (2016).
[35] H. Li, Q. Zhang, C. C. R. Yap, B. K. Tay, T. H. T. Edwin, A. Olivier, and D. Baillargeat, Adv. Funct. Mater. **22**, 1385 (2012).
[36] See Supplemental Material at http://link.aps.org/supplemental/10.1103/PhysRevB.102.115149 for more details about experimental data and calculations.
[37] W. McMillan, Phys. Rev. B **14**, 1496 (1976).
[38] A. Soumyanarayanan, M. M. Yee, Y. He, J. Van Wezel, D. J. Rahn, K. Rossnagel, E. W. Hudson, M. R. Norman, and J. E. Hoffman, Proc. Natl. Acad. Sci. USA **110**, 1623 (2013).
[39] S. Tang, C. Zhang, C. Jia, H. Ryu, C. Hwang, M. Hashimoto, D. Lu, Z. Liu, T. P. Devereaux, Z. X. Shen *et al.*, APL Mater. **6**, 026601 (2018).